Strain-Hardening Effects in BCC, FCC, and HCP Metals Loaded at Very High Rates

C. L. MEYERS JR

Gulf General Atomic Incorporated, San Diego, California, USA

Plastic deformation in typical bcc, fcc and hcp metals has been studied as a function of initial impact energy (up to about 4200 J). Materials included 1100-F aluminium, 2024-T3 aluminium, lead, OFHC copper, type-200 nickel, columbium, tantalum, vanadium, molybdenum, and cadmium. Macroscopic deformation resulting from projectile impacts at velocities up to 8 km/sec was recorded by sub-microsecond photography and flash X-radiography. A correlation was established between homologous test temperature (T/T_m) and size of craters resulting from impact, as was a relationship between the relative increase in microhardness in the impact affected region beneath the target crater and impact stress over the square root of compressibility. The microstructures of impulse-loaded regions were correlated with the stress levels effecting them. Strain profiles beneath the impact position for the type-200 nickel were determined metallographically and correlated with microhardness profiles.

1. Introduction

Considerable experimental research and numerous theoretical analyses have been performed since 1958, with regard to the deformation and fracture characteristics of metals and other structural materials which have been subjected to very-high-pressure impulse loads. Much of this past effort has had the objective of developing analytical means for describing material behaviour under hypervelocity impact conditions and for predicting results currently beyond the range of experimental capability. Such impact conditions are encountered when micrometeoroid particles impinge at very high relative velocities against orbiting satellites and space vehicles. Hypervelocity-particle encounters with manned structures in space can cause a variety of hazards and damage. However, one of the most significant is that of crater formation at the point of impact and of resulting hull penetration as the crater grows under the influence of very high impact stress. One of several recent reviews of hypervelocity impact studies has been presented by Gehring *et al* [1].

Analytical efforts to describe crater growth and the behaviour of target material subjected to shock-waves as a result of intense impulse loads, have resulted in several concepts of target material deformation. (i) Deformation by means of the formation of highly localised and short-lived "plasmatic" regions produced within the material behind the shock front [2]; (ii) deformation by means of "supercritical shear stresses" produced within the material behind the shock front [3]; and (iii) deformation in a "hydrodynamic" manner in material converted temporarily by the shock front to the state of viscous fluidity [4-13].

Although differing in the details of deformation modes, all three of the concepts above share in common one novel idea. This idea may be stated as follows: for stress levels above some threshold value (or at sufficiently high energy densities) the deformation and flow of crystalline materials is not restricted to the limitations of dislocation motion and interaction with point, surface and other line defects as in normal solid behaviour.

Theoretical analyses in the field of shock-wave mechanics, supported by experimental results, have shown that as a result of compression caused by strong shock waves, solid matter is heated to very high transient temperatures sufficient to convert solid to liquid (or even to
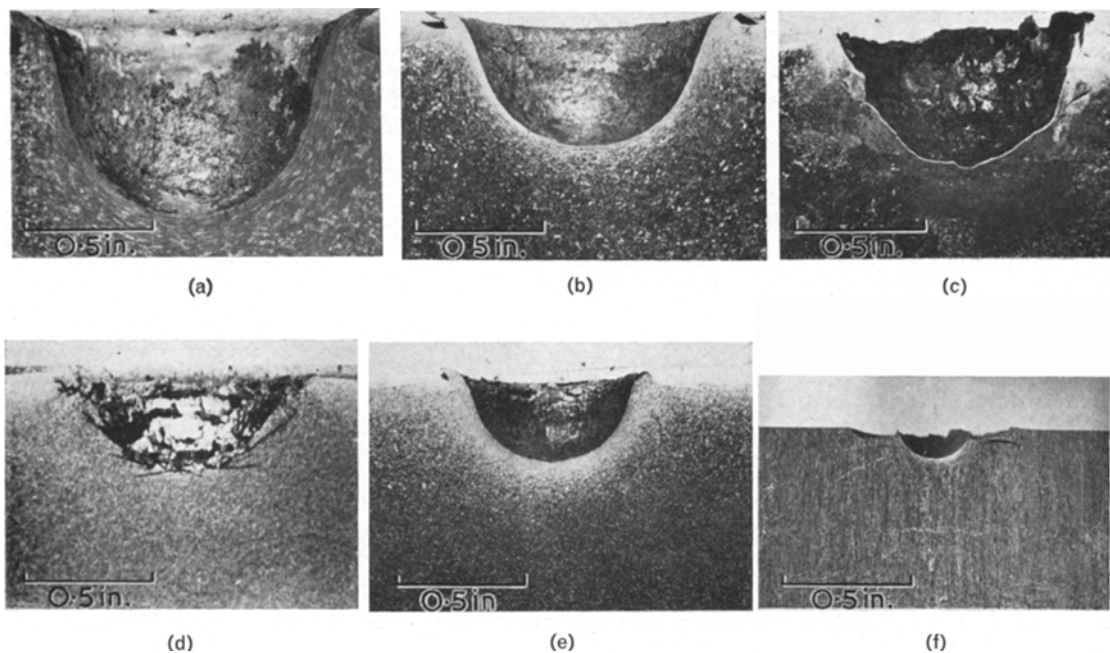
1

Figure 1 Macrophotos of crater sections in six metals, impact velocity 7 km/sec. (a) 1100F Al target crater; Cu target crater; (c) cp Cd target crater; (d) 2024-T3 Al target crater; (e) 200 Ni target crater; (f) Mo target

vapour) in the vicinity of an intense shock front [9]. Experimentally, Dieter [14] has shown that the strain-hardening effects of high-intensity shock waves on iron specimens (as observed by changes in microhardness) initially increase and apparently level off in the shock pressure range 270 to 310 kbar, with some uncertainty as to whether or not lower values of microhardness were observed for iron shocked at 270 kbar than for iron shocked at 220 kbar. In any case, an upper limit to shock-produced strain-hardening is suggested by these results. An additional implication is that for shock pressures above this strain-hardening limit, hydrodynamic flow would occur, possibly resulting in lower final hardening levels; i.e., there is sufficiently high energy density produced within the specimen to allow whole planes of atoms to move by laminar-flow as in the flow of a fluid. Theoretical analyses in the field of hypervelocity impact have applied the concept of the hydrodynamic flow of solids subjected to high-energy-particle impact to describe reasonably well the final shape and size of the resulting crater [4-10].

2. Experimental Procedure

Plastic deformation in metals representing the
*Plain carbon (0.18 %) steel.

2

bcc, fcc, and hcp crystal structures has been studied as a function of the initial impact energy [15, 16]. The bcc metals tested were columbium, tantalum, vanadium, molybdenum; the fcc metals were 1100-F aluminium, 2024-T3 aluminium, lead, OFHC copper, and 200 nickel; and a single hcp metal was cadmium. A summary of their physical and mechanical properties has been compiled in table I together with their compositions. Semi-infinite target blocks of these metals were loaded at very high rates by projectile impacts in a low-vacuum environment at velocities ranging between 4.3 and 7.9 km/sec (about 14000 to 26000 ft/sec). The projectiles were solid spheres of 1100 aluminium, C1018* steel, or Pyrex glass fired from a light-gas gun. Macroscopic deformation in target specimens was recorded during the process of hyper-velocity impact by means of sub-microsecond photographic equipment, supplemented by flash X-radiographic equipment. Details of projectile launching equipment and target instrumentation have been described in previous papers [15, 16].

3. Results and Discussion
3.1. Observations on Gross Deformation
Macrophotos of the gross deformation occurring

TABLE I Summary of Physical and mechanical properties ^{a} of metals studied.

Metal	Yield stress (psi* $\times 10^{-3}$)	U.T.S. (psi* $\times 10^{-3}$)	Hardness (DPH)	Specific gravity	Compress-ibility (psi^{-1}* $\times 10^6$)	Crystal-structure ^{b}	M.p. (°K)	Heat of fusion (cal/g)	b.p. (°K)	Heat of vaporisation (cal/g)
1100-F Al^c	6.4	13.0	27.0^h	2.70	0.105	fcc	933.0	93.0	2723.0	2510.0
2024-T3 Al^d	36.0^g	48.0^g	~145^h	2.90	0.102	fcc	~ 923	~96	~2673	~2510
OFHC Cu^e {HW-	14.3^h	28.3^h	58.0^h	8.96	0.046	fcc	1356.0	49.0	2868.0	1150.0
{RX-	13.7^h	28.1^h								
200 Ni (recrystallised)^f	30.0	70.0	~118^h	8.90	0.037	fcc	1726.0	72.0	3003.0	1550.0
c.p. Pb (as-cast)	1.6	2.6	(5.2, Bhn)	11.36	0.18	fcc	600.0	6.3	1998.0	223.0
Cb (annealed)	35.0	40.0	55.0	8.57	0.048	bcc	2741.0	69.0	5200.0	415.0
Ta (annealed)	~40	~ 50	(60 R$_E$)	16.6	0.033	bcc	~3269	38.0	~5698	1000.0
V (annealed)	64.0	72.0	(81 R$_B$)	6.1	0.026	bcc	~2173	79.0	3673.0	2080.0
Mo (annealed)	~57	~100	(156.0 Bhn)	10.22	0.030	bcc	2883.0	~70	5833.0	1340.0
cp Cd (as-cast)	53	7.3	20.0^h	8.65	0.093	hcp	594.0	13.0	1038.0	286.0

Notes (a) Room temperature values, except for last four columns. Nominal values from handbooks, unless otherwise designated.

(b) fcc: face-centred cubic; hcp: hexagonal close-packed; bcc: body-centred cubic.

(c) Commercially pure (99.0 min) aluminium. Formerly designated "2S".

(d) Aluminium-base alloy (3.5 to 4.5 % Cu, 0.4 to 1.0% Mn, 0.2 to 0.8% Mg). Formerly designated "24S". T3: solution-heat-treated and cold-worked; naturally aged to substantially stable condition.

(e) Oxygen-free high-conductivity copper. HW: hot-worked. RX: recrystallised.

(f) Commercially pure (99.50) nickel. Formerly designated "A".

(g) Vendor certification.

(h) GM DRL measurements.

*psi units are used in this table. 1.0 psi = 1.0 lb/in.² = 7 × 10^{-2} kg/cm².

during crater growth are shown in fig. 1. The lip around the crater develops as target material flows rapidly radially, then backward around the impacting projectile. Crater growth has been observed to consist of two types of metal displacement. The more significant type is similar to the flow occurring during a back-extrusion operation, as performed by conventional metalworking methods; the other, amounting to between ~2 and ~20% of the total mass displaced, is the loss of mass by the ejection of vapourised, molten, and/or fragmented solid metal [15]. As is illustrated in fig. 1, the ductile metals (1100 aluminium, OFHC copper and 200 nickel) retain well-formed crater lips, whereas the low-elongation metals (cadmium, molybdenum and 2024-T3 aluminium) exhibit lip spall and internal cracking.

As shown in fig. 2, crater diameters were plotted from successive film frames as a function of time for the weak 1100-F and the strong 2024-T3 aluminium alloys, as well as for OFHC copper, 200 nickel and cadmium. These craters were formed from single impacts by 0.476 cm-diameter spherical projectives of 1100 aluminium striking the targets at 7.1 to 7.4 km/sec, resulting in impact energies of approximately 4125 J each.
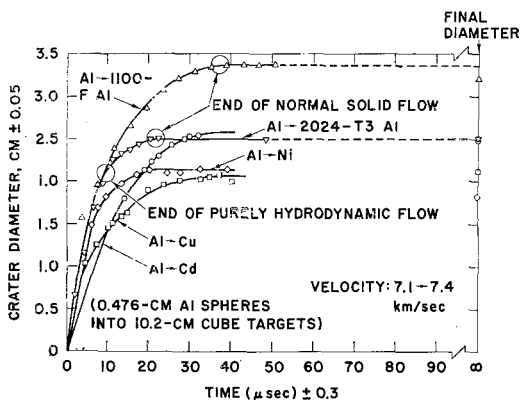

Figure 2 Impact crater-growth in copper, nickel, cadmium, and two aluminium-base metals.

Initially the crater growth in both aluminium targets seems to behave in essentially the same way, flowing with a viscosity determined by the physical properties of the base metal and without any apparent differences in normal solid strength levels. At about 10 μsec after impact, the growth-rates of the two materials begin to diverge at the end of the régime of purely hydrodynamic

flow. Crater-growth has been arrested earlier in the 2024 aluminium target, as would be intuitively expected by virtue of its higher strength level in the normal solid state than that of 1100 aluminium. The end of the régime for normal solid flow in these targets has been assumed where crater-diameter has become unchanging with time. (A small amount of dimensional recovery due to combined elastic and anelastic behaviour was exhibited by the craters in 1100 aluminium, in 200 nickel, and in cadmium.) Thus, strain-hardening should not occur during the hydrodynamic régime of flow – not until the energy density beneath the region of impact has dropped below some energy density (or stress amplitude) threshold which remains to be determined. Strain-hardening was observed subsequently in these two aluminium materials, occurring during the passage of the lower energy "tail" of the stress wave (and also while the amplitude of wave falls below the hydrodynamic flow threshold owing to internal energy losses). These and other observations reveal that all deformation associated with impact-generated craters generally occurs within ~50 microseconds after impact.

Crater-growth behaviour for OFHC copper and for 200 nickel, also appears somewhat similar to the behaviour previously discussed. Since copper and nickel have densities and hugoniots which differ from each other by only a small percentage (analogous to the case for 1100 aluminium and 2024 aluminium alloy), the superposition of their crater-growth curves during the régime of purely hydrodynamic flow is not surprising. Although the density of cadmium is close to that of copper and of nickel, its hugoniot differs appreciably from theirs; consequently, the initial rate of crater-growth differs from that for copper and nickel. These hypervelocity impact studies have shown that, although the initial deformation behaviour (during the hydrodynamic régime) may be similar for certain different target materials, the ultimate extent of target deformation is governed by strain-hardening effects which follow the peak of the stress wave and which are characteristic of each metal.

Fig. 3 illustrates that the average initial rates of crater-growth show essentially no dependence on normal solid properties (represented by target homologous test temperature), as would be expected for hydrodynamic (non-strain-hardening flow). If the asserted hydrodynamic
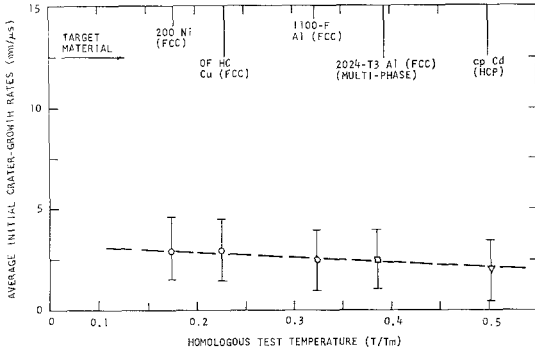
4

Figure 3 Initial crater-growth rates in two aluminium-base metals, copper, nickel, and cadmium as a function of target metal homologous test temperature.

flow behaviour is compared with the behaviour of a Newtonian fluid for the metals shown in fig. 3, then analogous relationships become apparent. For a shock-loaded target, the average initial rate of crater-growth (increase in crater diameter, D_c, with time after impact) during the hydrodynamic-flow régime can be related to particle velocity, u, within the shock-loaded solid;

$$\frac{\mathrm{d}}{\mathrm{d}t}(D_c) \approx u = C_1 \sigma_I \qquad (1)$$

wherein σ_I is the initial shock stress and C_1 is $(V\rho_0)^{-1}$; V is the impact velocity, a constant for any given test; and ρ_0 is the initial target density, also a constant. However, the hydrodynamic flow of the target material can be compared as well with that for a Newtonian fluid which is described as follows:

$$\frac{\mathrm{d}}{\mathrm{d}t}(D_c) \approx \dot{\epsilon} = \sigma/C_2 \qquad (2)$$

wherein $\dot{\epsilon}$ is the strain rate (or rate of flow), σ is the applied stress and C_2 is a proportionality coefficient (apparent viscosity). Table II tabulates data from fig. 3 and [17] to estimate values for C_2, the apparent viscosity of the target "fluid" during hydrodynamic flow.

Fig. 4 illustrates later effects in terms of final crater diameter for 1100-F aluminium, cadmium, OFHC copper and 200 nickel targets. The final crater-diameters shown in these figures are mutually consistent with the normal solid mechanical properties, as shown in table I. The other dimensions of the crater (depth and volume) show similar results. These results exhibit an apparent sensitivity to prior strain-hardening within the target metal. For example, the copper targets impacted were in two different conditions: hot-worked (HW) and fully recrystallised (RX). The splitting of the curve for Al→Cu in fig. 4 illustrates this effect well. The order of the curves shown in this figure, from uppermost to
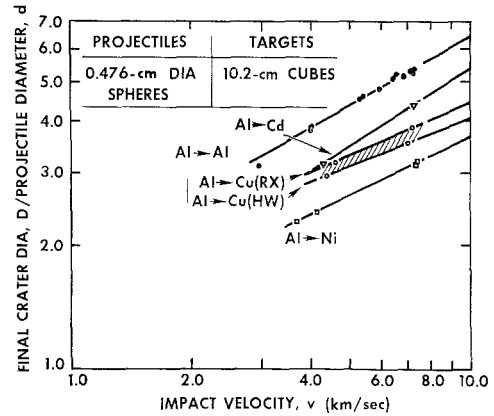

Figure 4 Crater final diameters in aluminium, copper, nickel, and cadmium targets as a function of projectile impact velocity.

TABLE II Computation of apparent viscosity of metals during hydrodynamic flow[a].

Target metal	$\sigma_I \approx \sigma$ (M bars)[b]	$\dot{\epsilon}_{av} \approx \frac{d}{dt}(D_c)$[c]	C_2, apparent viscosity (mm³/gm sec)	Remarks[d]
1100-F Al	1.05	2.5	25.0	⎫ Both fcc; same
2024-T3 Al	~1.05	2.5	25.0	⎰ χ_0 and ρ_0
OFHC Cu	1.63	3.0	19.0	⎫ Both fcc; same
200 Ni	1.60	3.0	19.0	⎰ χ_0 and ρ_0
cp Cd	1.53	2.0	13.0	hcp; same ρ as Cu & Ni, but different χ_0

Notes (a) Estimation of C_2-parameter in equation 2.
(b) σ_I is initial shock stress (in Mbar); σ is applied stress.
(c) $\dot{\epsilon}_{av}$ is average rate of material flow estimated from curves in fig. 2 and plotted in fig. 3.
(d) χ_0 is initial compressibility; ρ_0 is initial density. fcc: face-centred cubic; hcp: hexagonal close-packed.

lowest, correlates with an increasing order of initial stress at impact: 0.98, 1.35, 1.50, and 1.53 Mbar for the Al, Cd, Cu, and Ni targets, respectively.

One of several possible empirical correlations relates final crater parameter $\Phi = D_i/d$, to the target metal's homologous test temperature (for unalloyed metals and for negligible amounts of initial strain-hardening);

$$\Phi = D_i/d \approx \beta' \, (T/T_m) \qquad (3)$$

wherein D_i is the final inner diameter of the crater; d is the projectile diameter; T is the test temperature (°K); T_m is the target-metal's melting temperature (°K).

Figure 5 Correlation of β^1-parameter with target metal crystal-structure.

TABLE III Comparison of β^1 values for target metals[a].

Target metal	β' Value in eqn. 1	Relative values of β'	Crystal-structure[b]
1100F Al	16.4	2	fcc
OFHC Cu	17.4	2	fcc
200 Ni	18.1	2	fcc
cp Cd	8.7	1	hcp

Notes (a) Data from fig. 4 at ~7.3 km/sec.
(b) fcc: face-centred cubic; hcp: hexagonal close-packed.

Experimental data from fig. 4 taken at an impact velocity of ~7.3 km/sec yield values for coefficient β' in equation 3 which are shown in table III, along with the characteristic crystal-structure of the target metal. A more general correlation of the β' parameter with metal-crystal structure is shown in fig. 5 for a number of targets. The scatter band widths are essentially a function of degree of divergence from identical impact conditions; i.e. differences in projectile materials and sizes and in impact velocities. (The Ni, Cu and Al groups at ~4125 J show little scatter because (i) identical projectiles were used, and (ii) impact velocities were held within a range of 7.1 to 7.4 km/sec.) However, the grouping of the data by crystal-structure is quite evident. The relative values of β' seem to bear some relation to the number of slip systems ideally available for plastic flow for each crystal-structure.

3.2. Metallographic Observations

A comparison of strain-hardening effects beneath craters formed in six target metals is shown in fig. 6. The differences exhibited between mi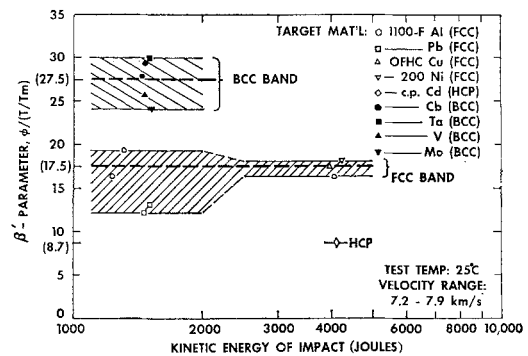cro-hardness profiles arise during the normal solid flow régime at the tail end of crater-growth, and have their origin in the differences between these metals in normal mechanical behaviour. The relative order of the microhardness "peaks" shown in this figure is consistent with the order for crater diameter shown in fig. 4 for four of the target metals. "peak height" has been found empirically to be described by

$$\frac{\delta \, (DPH)}{(DPH)_2} = \psi \, \frac{\sigma_I}{\chi^{1/2}} \qquad (4)$$

where $(DPH)_I$ = pre-impact microhardness; $\delta(DPH)$ = "peak height"; σ_I = initial impact stress; χ = target metal compressibility; ψ = proportionality factor: ~1 for fcc; ~0.3 for hcp and for bcc.

Calculated values for ψ are compiled for five target metals in table IV. The steep initial rise in microhardness at the crater bottom for these curves is independent of indenter load and, therefore, should not be a result of measurement technique. The "peaks" have been attributed to the effect of shock-heating which causes varying amounts of recovery or recrystallisation in the region adjacent to the crater during crater-growth [9, 18]. The unaltered microhardness profiles would not manifest these "peaks", and the curves in fig. 6 would extrapolate upward and to the right upon approaching the crater wall.

The microhardness profiles beneath impact positions, described above, were correlated with macro-/microstructures and with the estimated variation of stress-wave amplitude with distance from impact. The observations for 200 nickel revealed that the effects of strain-hardening extend only a few millimetres beneath the crater,
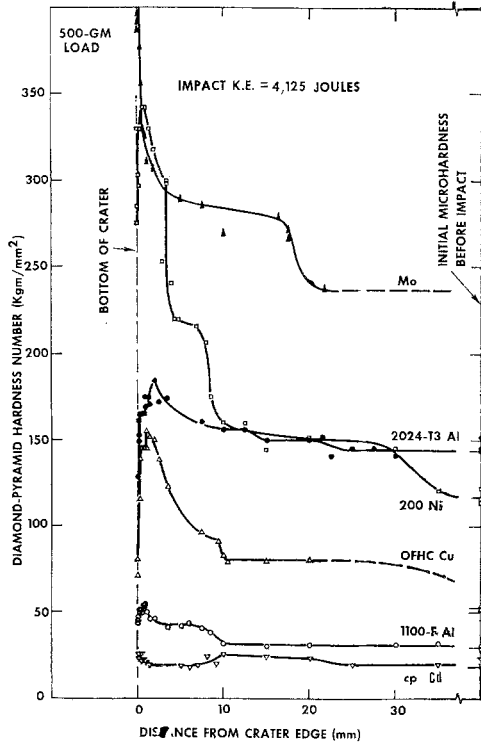
6

Figure 6 Micro-indentation hardness profiles of impact-affected regions in six target metals.
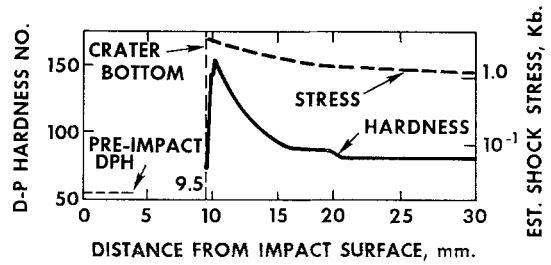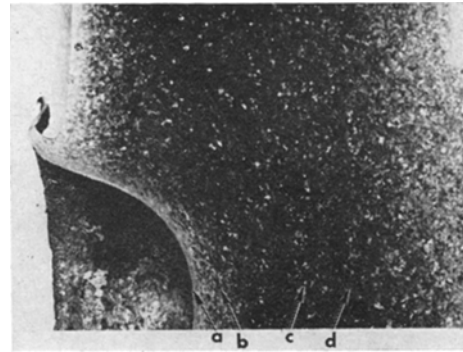

Figure 7 Macrostructure and micro-indentation hardness profile of impact-affected region in OFHC copper target.

the most severe deformation observed within the first millimeter. No recrystallisation was noted within the deformed zone below the nickel crater. Similar behaviour was observed for both the 1100-F and 2024-T3 aluminium alloys. However, some recrystallisation by shock-heating effects was evident within the impact-affected region for both the copper and cadmium targets, as is illustrated in fig. 7 and 8 for the copper target. The superposed stress distribution was estimated by assuming an exponential decay in stress from a maximum value at impact, as determined from the appropriate hugoniot curves [17],

down to a value calculated for the uniaxial-strain yield stress.

A strain profile, illustrated in fig. 9, beneath the nickel-target crater was estimated by a comparative method. The nickel-target specimen and the reference nickel tensile specimen were first recrystallised together at 588° C for 45 min, after both had been strain-hardened to "failure" and microhardness profiles determined. Micro-hardness profiles for the target and the tensile specimens appear to be similar, except that the curve for the tensile specimen is horizontally compressed and exhibits considerable scatter near its origin. The superposed stress distribution for the nickel-target specimen was estimated

TABLE IV Calculated values for ψ^* for five metal impact targets.

Target metal	$\dfrac{\delta \text{ (DPH)}}{\text{(DPH)}_0}$	σ_I (Mbar)	$\chi^{1/2}$ (Mbar)$^{-1/2}$	ψ (Mbar)$^{-3/2}$	Crystal-structure
200 Ni	2.05	1.63	0.77	0.97	fcc
OFHC Cu	1.82	1.60	0.82	0.94	fcc
1100 Al	0.86	1.05	1.24	1.02	fcc
Cd (cp)	0.35	1.53	1.17	0.27	hcp
Mo (P & S)	0.70	1.63	0.66	0.29	bcc

*Calculations based upon $\psi = \dfrac{\delta \text{ (DPH)}}{\text{(DPH)}_0} \dfrac{\chi^{1/2}}{\sigma_I}$
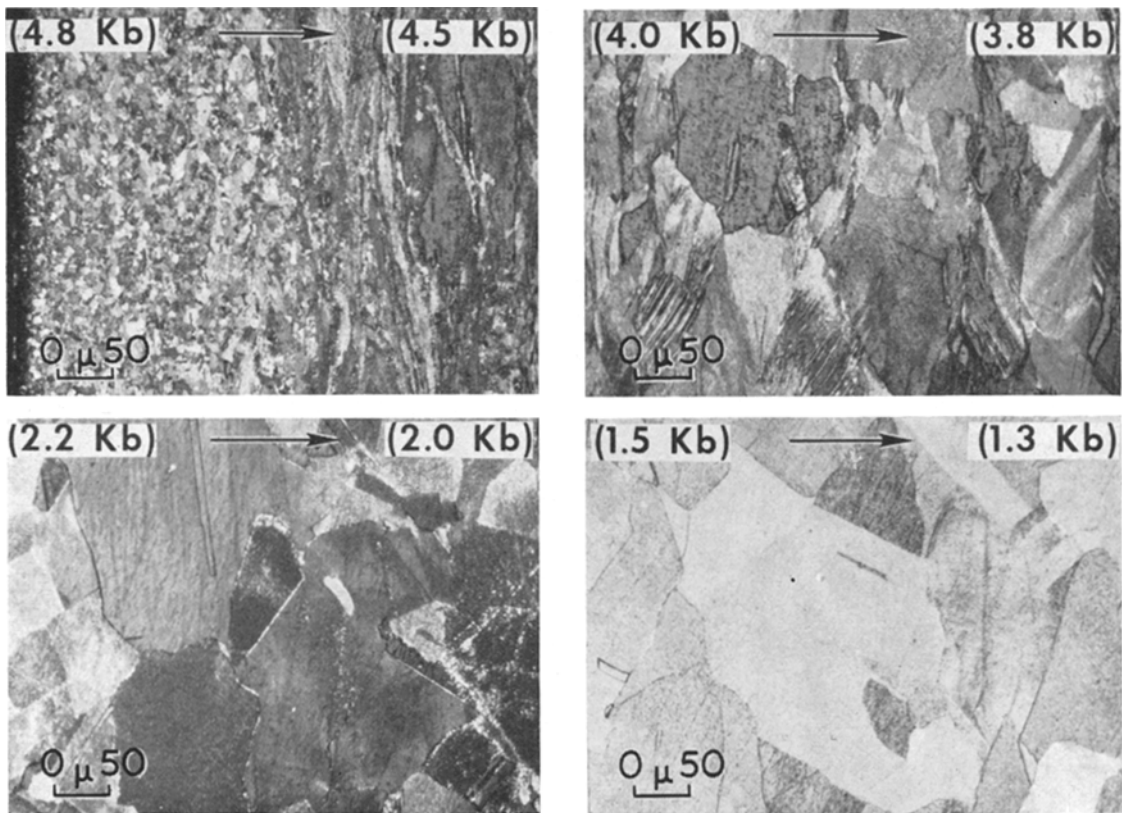
Figure 8 Microstructures of fields designated in fig. 7 for OFHC copper target.

in the same manner as that shown in fig. 7 for the copper target. The stress distribution for the tensile specimen was calculated from measurements of the load at failure and the variation in cross-sectional area with distance from the fracture surface. Both stress distribution in the tensile specimen was calculated in cumulative increments from a graphical comparison of initial and final specimen shape and size. The strain distribution in the target specimen was then determined by microstructural and micro-hardness comparisons of the two specimens, after the method of Mobley and Pond [19]. Transitions of similar character were matched within the two microstructures and identified as reference positions (a), (b), and (c), for which strain values were determined from the underlying tensile specimen strain profile. These three strain-value estimates were used to construct a strain profile for the target specimen. The strain profiles seem to be linear for both, with the strain profile for the target specimen slightly exceeding unity at the crater edge where the

microstructure essentially has been obliterated by the very high degree of deformation produced by the tail of the stress wave.

4. Summary

Strain-hardening resulting from hypervelocity projectile impacts (up to ∼8 km/sec) was studied as a function of initial impact energy for target metals representing the bcc, fcc, and hcp crystal-structures. A concept of the hydrodynamic flow of materials has been utilised to describe target deformation during the initial phase of hyper-velocity impact. The resulting crater size in a given target metal has been shown to increase essentially linearly with impact velocity. A comparison of these curves for the several target metals studied has shown a correlation between magnitude of crater-diameter plotted and initial stress at impact. Furthermore, an empirical correlation has been made of crater-size with the physical properties of the target metals.

Microhardness surveys for strain-hardening

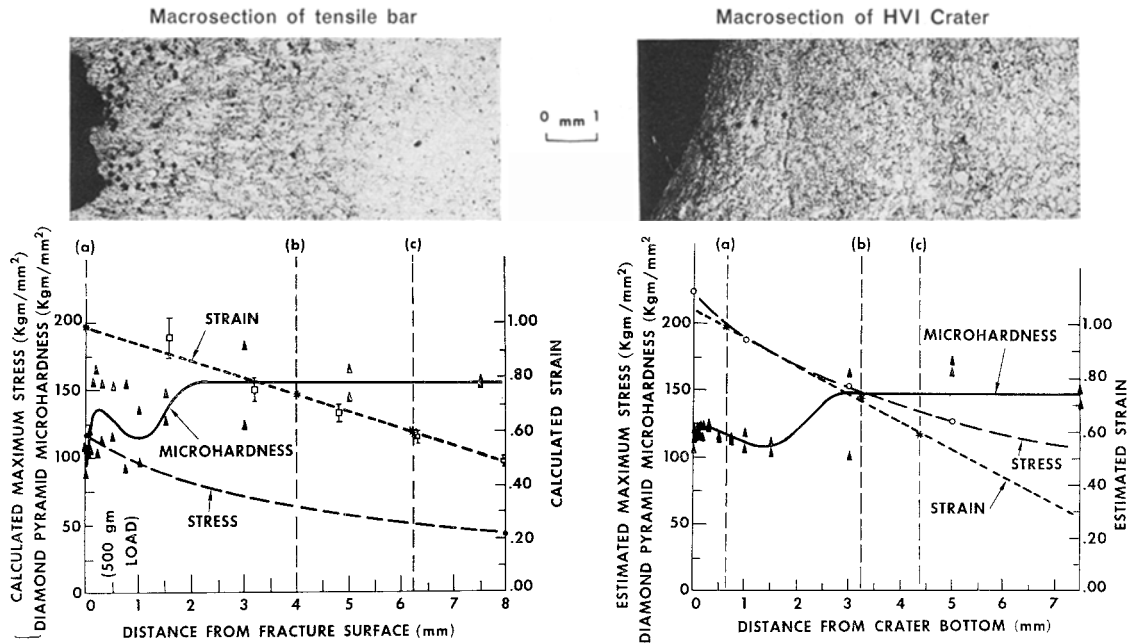Macrosection of tensile bar   Macrosection of HVI Crater

Figure 9 Comparison of microstructures with micro-indentation hardness, strain and stress profiles within type-200 nickel target crater and tapered tensile specimen.

effects beneath craters formed by hypervelocity impact have shown that the resultant relative hardening is proportional to the initial stress amplitude at impact and inversely proportional to the square root of the target metal compressibility. The microhardness profile for the nickel target was correlated with its microstructure and with the estimated variation of stress-wave amplitude with distance from impact. A strain profile was estimated for the impact-affected region beneath the nickel crater.

Acknowledgements

References

1. J. W. GEHRING, C. L. MEYERS, and K. H. MEYER, TR-W13-5-65, American Society for Metals, Metals Park, Ohio (February, 1965).
2. A. BURKHARDT, Mitteilungen (no. 1/2) p.2. (25 January, 1964).
3. G. R. COWAN, Trans. Met. Soc. AIME 233 (1965) 1120.
4. R. J. BJORK, The Rand Corp. Report No. P-1662 (16 December, 1958).
5. Idem, Proc. 6th Hypervelocity Impact Symposium,
II-1 (Firestone Tire and Rubber Co., Cleveland Ohio, 30 April-2 May 1963) p. 1.
6. J. M. WALSH and J. H. TILLOTSON, ibid p. 59.
7. T. E. RINEY, ibid p. 105.
8. M. L. WILKINS and R. GIROUX, ibid p. 141.
9. R. L. BJORK and A. E. OLSHAKER, The Rand Corp. Memo No. RM-3490-PR (May, 1965).
10. F. E. ALLISON, Proc. 7th Hypervelocity Impact Symp., Vol. 5. (Martin Co, Orlando, Florida, 1965) p. 213.
11. A. M. DIETRICH, R. B. POND, and C. M. GLASS, ibid, Vol. 5, p. 1.
12. S. M. HALPERSON, ibid, Vol. 5, p. 235.
13. J. N. GOODIER, ibid, Vol. 3, p. 215.
14. G. E. DIETER, "Response of Metals to High Velocity Deformation" (Met. Soc. Conf. Vol. 9, Interscience, New York, 1960), p. 421.
15. C. L. MEYERS, J. A. CHAREST, C. J. MAIDEN, and J. W. GEHRING, TR64-48 GM Defence Research Laboratories, Santa Barbara, Calif. (September, 1964).
16. J. W. GEHRING, C. L. MEYERS, and J. A. CHAREST, Proc. 7th Hypervelocity Impact Symp., Vol. 5 (Martin Co, Orlando, Florida, 1965) p. 161.
17. R. G. MCQUEEN and S. P. MARSH, J. Appl. Phys. 31 (1960) 1253.
18. E. P. PALMER and G. H. TURNER, Proc. 7th Hypervelocity Impact Symp., Vol. 5 (Martin Co, Orlando, Florida, 1965) p. 13.
19. C. B. MOBLEY JR. and R. B. POND ibid, Vol. 5, p. 73.